

Quantum Trajectory-Electronic Structure Approach for Exploring Nuclear Effects in the Dynamics of Nanomaterials

Sophya Garashchuk,^{*,†} Jacek Jakowski,^{*,‡} Lei Wang,[†] and Bobby G. Sumpter[§]

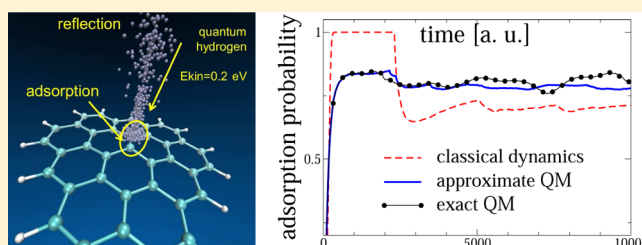
[†]Department of Chemistry and Biochemistry, University of South Carolina, Columbia, South Carolina 29208, United States

[‡]National Institute of Computational Sciences, University of Tennessee, Oak Ridge, Tennessee 37831, United States

[§]Center for Nanophase Materials Sciences and Computer Science and Mathematics Division, Oak Ridge National Laboratory, Oak Ridge, Tennessee 37831, United States

S Supporting Information

ABSTRACT: A massively parallel, direct quantum molecular dynamics method is described. The method combines a quantum trajectory (QT) representation of the nuclear wave function discretized into an ensemble of trajectories with an electronic structure (ES) description of electrons, namely using the density functional tight binding (DFTB) theory. Quantum nuclear effects are included into the dynamics of the nuclei via quantum corrections to the classical forces. To reduce computational cost and increase numerical accuracy, the quantum corrections to dynamics resulting from localization of the nuclear wave function are computed approximately and included into selected degrees of freedom representing light particles where the quantum effects are expected to be the most pronounced. A massively parallel implementation, based on the message passing interface allows for efficient simulations of ensembles of thousands of trajectories at once. The QTES-DFTB dynamics approach is employed to study the role of quantum nuclear effects on the interaction of hydrogen with a model graphene sheet, revealing that neglect of nuclear effects can lead to an overestimation of adsorption.



1. INTRODUCTION

During the last couple of decades significant theoretical and experimental efforts have been devoted to studies of adsorption of light molecules in nanoporous materials. The interest comes from applications in molecular sieving,^{1–4} fuel cells,^{5–7} and hydrogen storage⁸ among others. Carbon allotropes, having low mass density and tunable electrical, mechanical, and thermal properties, are particularly attractive materials for applications ranging from graphite used in the plasma-facing components in a fusion reactor, to porous carbon used for hydrogen storage or battery electrodes, to graphene considered for sensors and numerous electronics applications.^{1–4,8–12}

The quantum nature of light nuclei adsorbed on porous surfaces and its potential role in designing advanced materials with tailored properties is being increasingly recognized. For example, full description of proton transport through a proton exchange membrane of a fuel cell and through water-filled channels in a carbon nanotube requires quantization of the proton states.^{5–7,13,14} In quantum sieving the difference between the zero-point energy (ZPE) of hydrogen isotopes and delocalizations of their quantum states allows efficient separation of H₂ over D₂ and T₂ in zeolites and porous carbon. The observed isotope selectivity is in the range of 10–500 (depending on the temperature) for D₂ and H₂ in zeolites, and it can be as high as 10⁵ for a mixture of T₂ and H₂ in carbon nanotubes.^{1–4,15–18}

Nuclear motion and the isotope effect can also play a key role in modulating electronic structure and subsequent performance of molecular devices. For example, the processes responsible for efficiency of light-harvesting in organic solar cells are in part driven by the nuclear motion which modulates the energy matching between the electron donor and acceptor. This modulation effect cannot be fully described if the nuclei are treated as purely classical particles.¹⁹ Deuteration of the side chain of poly(3-hexylthiophene), P3HT, in a photovoltaic heterojunction can significantly reduce the open circuit voltage without noticeable changes in the structure of a heterojunction.²⁰ Nuclear motion may also influence the sensitivity of the electronic properties of a single graphene sheet to defects in crystal structures, which may change hybridization. The effect of vibrational modes on the electronic properties of graphene-based materials is of particular importance^{21–26} and may be used to design highly sensitive detectors.^{11,12}

Conceptually, conventional molecular dynamics approaches describing nuclei as classical particles are appropriate in many situations.^{27,28} However, inclusion of the quantum-mechanical (QM) effects, such as the ZPE, tunneling and nonadiabatic transitions, is necessary for understanding of chemical processes at low energy or temperature, even in large molecular systems or in the condensed phase. For example, QM tunneling is

Received: July 12, 2013

Published: November 12, 2013



known to dominate proton transfer at low temperature in biological environments.^{29–31} In the area of bond-selective chemistry, intermode energy flow and ZPE should be considered for understanding effects of the vibrational excitation on bond breaking.^{32,33} In quasi-classical trajectory simulations for example, it is necessary to include the rovibrational ZPE to reach the saddle point in the association reaction of H with acetylene;³⁴ ZPE should also be included and constrained to prevent nonphysical dissociation of the water dimer and trimer.^{35,36} Thus, incorporation of nuclear QM effects and assessment of their role in chemical dynamics is highly desirable.

For general molecular systems the numerical cost of exact QM time-dependent methods of solving the Schrödinger equation, that are based on basis or discrete variable representation,³⁷ scales exponentially with the system size. By contrast, the numerical cost of classical trajectory dynamics scales linearly. In order to develop methodologies suitable for large molecular systems and incorporate QM effects for, at least, some of the nuclei, considerable efforts have been devoted to the trajectory-based mixed quantum/classical or semiclassical dynamics for the *nuclei* combined with a practical approach for computing electronic structure on-the-fly. Here the word “practical” means applicable to systems of hundreds of atoms, yet accurate and general, i.e., able to treat reactive processes in the condensed phase. References 38–47 describe some of these methodologies; however, there is no widely accepted general approach, as established as molecular dynamics in classical simulations. Semiclassical and mixed quantum/classical methodologies are hard to extend to the exact limit of quantum mechanics. For example, ring polymer molecular dynamics^{48,49} has some very impressive applications but is derived from heuristic arguments. The semiclassical initial value representation can be improved by wave function re-expansions, but this is never done in practice, since the procedure scales quadratically with respect to the number of trajectories (to the contrary, in high-dimensional applications an additional linearized, or forward–backward, approximation is made). The path integral methods, such as path integral Monte Carlo and path integral molecular dynamics, add effects of quantum dispersion into statistical and thermodynamic properties of large molecular systems.^{50–52} However, these methods are not well-suited to model processes in real time on a “single-molecule” level.

The method, described in this paper, is a hybrid of approximate quantum trajectory (QT) dynamics with electronic structure (ES) calculations performed on-the-fly. Specifically, the self-consistent charge density functional tight binding (SCC-DFTB) electronic structure method^{53–56} is employed. This hybrid approach will be referred to as QTES-DFTB dynamics. The quantum corrections for the nuclei are incorporated into selected degrees of freedom (DoFs), providing a mixed quantum/classical description of the nuclei, developed within the QT framework.⁵⁷

In general, the trajectory representation of large molecular systems is appealing for conceptual and practical reasons: (i) Classical mechanics is often adequate for the description of nuclear motion of many thousands of atoms.²⁸ Thus, it may serve as a starting point for approximate methods, which incorporate the dominant QM effects either by using information of the classical trajectories, as done in the semiclassical and quasiclassical methods, or by making corrections to the dynamics itself as, for example, in the

centroid dynamics⁴⁴ or approximate QT dynamics.⁵⁸ (ii) The trajectory framework, used for both light and heavy—or quantum and classical—particles, provides equal treatment of all the nuclei and alleviates problems of the quantum-classical separation of the DoFs.⁵⁹ (iii) Unlike conventional wave function representations, the trajectories are well-suited to capture highly oscillatory behavior of a wave function near the classical limit $\hbar \rightarrow 0$ and are convenient for parallelization.

In the quantum, also called Bohmian, trajectory formalism, a wave function is represented by an ensemble of trajectories moving according to Newton’s laws of motion. The QM correction to the dynamics comes from the quantum force which acts in addition to the external or “classical” force of electronic interactions. The nonlocal quantum potential, formally generating all quantum effects in a system, is an easily identifiable object of approximations ranging from classical (the quantum potential set to zero) to the full quantum (highly accurate quantum potential) dynamics limits. Some level of approximation of the quantum potential is necessary to avoid exponential scaling of the numerical cost with dimensionality, and it makes physical sense to do so for heavy particles such as nuclei. Changing the quantum potential between the classical limit and simple approximations (such as implemented in this work) can be useful for determining if the quantum effects are important, if they can be reproduced by the independent-trajectory methods etc.

Quantum nuclear dynamics studies of large reactive systems is impossible without a highly efficient treatment of the electronic structure, which is by far the most expensive computational step of the dynamics. The electronic structure calculations, implemented here within SCC-DFTB as a middle-ground between accuracy and numerical cost, are distributed using a message passing interface across multiple computing nodes. The quantum force is computed *approximately* from average properties of the ensemble. Computation of the average quantities and other observables of interest is performed sequentially and requires passing trajectory information (positions, momenta, action functions) to a head computing node. Each computing node can utilize open message passing multithreading to evaluate energy and forces. Thus, the QTES dynamics can be parallelized in an efficient and straightforward manner.

This paper is organized as follows: Section 2 outlines the approximate QT formalism, the mixed quantum/classical framework for the nuclear DoFs and implementation of the DFTB employed in the QTES code, which is used to propagate thousands of trajectories for hundreds of DoFs in parallel. In section 3 the QTES-DFTB is applied to study collisions of atomic hydrogen with a graphene “fragment”, C₃₇H₁₅, including analysis of the DFTB accuracy and studies of adsorption probability with and without the quantum correction. Section 4 concludes.

2. METHODOLOGY AND IMPLEMENTATION

To perform rigorous quantum molecular dynamics one has to solve the time-dependent Schrödinger equation (TDSE) for both electrons and nuclei. However in most cases, one takes advantage of the electron/nuclei mass separation and invokes the Born–Oppenheimer approximation. In this case, the total wave function is represented as a product of the nuclear and electronic wave functions,

$$\Psi = \psi_{\text{nuclei}} \phi_{\text{electrons}}$$

and it is assumed that electrons are describable by a single stationary electronic state. This state is a solution to the time-independent Schrödinger equation in the potential of charges of the space-fixed nuclei. This electronic energy combined with the nuclear repulsion for various nuclear geometries gives the electronic potential energy surface (PES) V , governing the motion of nuclei.

The Born–Oppenheimer framework is generalizable to a few (two to four) electronic states but becomes impractical if a multitude of electronic states has to be considered. Therefore, alternative time-dependent treatments of electrons have been developed, in most cases in conjunction with the *classical* treatment of the nuclei, such as the electron–nuclear dynamics,⁶⁰ the Liouville–von Neumann dynamics,⁶¹ the time-dependent density functional theory (DFT), quantum wave packet ab initio molecular dynamics.⁶² While QM electron–nuclear dynamics will be considered in the future, in the present paper we work within the Born–Oppenheimer approximation and, furthermore, for scalability to large systems, we make use of the mass separation between the light and heavy nuclei. More precisely, we distinguish between the nuclei for which QM effects are expected to be significant, the so-called light or quantum nuclei, and the nuclei likely to behave classically, the so-called heavy or classical nuclei, to formulate a mixed quantum/classical nuclear dynamics within the quantum trajectory (QT) approach summarized in section 2.2. Before proceeding with the presentation of the formalism, we emphasize that compared to traditional molecular dynamics describing nuclei in terms of a single classical trajectory, in the QT dynamics a wave function is represented by an ensemble of trajectories that evolve simultaneously under the combined action of classical and quantum forces. The latter force, computed from the trajectory ensemble for practical reasons approximately, incorporates nonlocality of quantum mechanics into a trajectory dynamics framework.

2.1. Quantum Trajectory Formalism. The quantum trajectory (QT) formalism is presented for a general multi-dimensional quantum system described in full Cartesian space, followed by an adaptation for a molecular system comprised of light and heavy nuclei. The positions of N_p quantum particles are sequentially arranged into a column-vector \vec{x} of dimensionality $N_d = 3N_p$; a diagonal matrix of inverse particle masses $\{m_1, m_2, \dots, m_{N_p}\}$ is denoted \mathbf{G} ,

$$G_{11} = G_{22} = G_{33} = m_1^{-1}, \quad G_{44} = G_{55} = G_{66} = m_2^{-1} \dots \quad (1)$$

The range of integration for each spatial coordinate is $[-\infty, \infty]$. The gradient, ∇ , is a column-vector of spatial derivatives

$$\nabla = \begin{bmatrix} \frac{\partial}{\partial x_1} \\ \frac{\partial}{\partial x_2} \\ \vdots \\ \frac{\partial}{\partial x_{N_d}} \end{bmatrix} \quad (2)$$

The subscript label t indicates quantities associated with the trajectories. Generalization of the QT formalism to arbitrary coordinate systems has been given elsewhere.⁶³

The wave function evolution is governed by the TDSE with the time-independent potential, V , which will be referred to as “classical”

$$i\hbar \frac{\partial}{\partial t} \psi(\vec{x}, t) = \hat{H}\psi(\vec{x}, t) \quad (3)$$

The operator \hat{H} is the usual QM Hamiltonian,

$$\hat{H} = -\frac{\hbar^2}{2} \nabla^T \cdot \mathbf{G} \cdot \nabla + V(\vec{x}) \quad (4)$$

in which the first term is a kinetic energy written in matrix notation and the second term is a potential energy. The superscript T indicates the transpose of a column-vector, so that the ∇^T is a row-vector. The QT approach is based on the Madelung–de Broglie–Bohm (also called Bohmian or hydrodynamic) formulation of the TDSE.^{64,65} The wave function is written in the polar form,

$$\psi(\vec{x}, t) = A(\vec{x}, t) \exp\left(\frac{i}{\hbar} S(\vec{x}, t)\right) \quad (5)$$

in terms of a non-negative amplitude A , and of a real phase S . Functions A and S are both scalars. Substituting eq 5 into the TDSE eqs 3 and 4, identifying the trajectory momentum \vec{p} with the gradient of the phase,

$$\vec{p} = \nabla S \quad (6)$$

and switching to the Lagrangian frame-of-reference

$$\frac{d}{dt} = \frac{\partial}{\partial t} + \vec{p}^T \cdot \mathbf{G} \cdot \nabla \quad (7)$$

one obtains the following $2N_d$ equations of motion for the quantum trajectories:

$$\frac{d\vec{x}_t}{dt} = \mathbf{G} \cdot \vec{p}_t \quad (8)$$

$$\frac{d\vec{p}_t}{dt} = -\nabla(V + U)|_{\vec{x}=\vec{x}_t} \quad (9)$$

Each trajectory is defined by its position \vec{x}_t and momentum \vec{p}_t . The dynamics of the QTs is governed by the combined influence of the classical potential V and the quantum potential U ,

$$U = -\frac{\hbar^2}{2A} \nabla^T \cdot \mathbf{G} \cdot \nabla A(\vec{x}, t) \quad (10)$$

The potential U is a nonlocal time-dependent function which couples evolution of multiple QTs representing a single wave function. Interaction of QTs mediated by the quantum potential is responsible for all QM effects in a system. Note, that the QT formulation is formally equivalent to the TDSE and has a natural *classical dynamics* limit of $U = 0$. The limit of vanishingly small quantum potential, i. e., $\hbar \rightarrow 0$ or infinite particle mass, is appropriate for heavy particles such as nuclei and will be invoked in section 2.2. The QTs representing a single wave function $\psi(\vec{x}, t)$ form an *ensemble*: all trajectories should be propagated concurrently for the quantum potential to be computed “on-the-fly”.

The wave function phase, S , along a trajectory evolves in time according to

$$\frac{d}{dt} S(\vec{x}_t) = \frac{1}{2} \vec{p}_t^T \cdot \mathbf{G} \cdot \vec{p}_t - (V + U)|_{\vec{x}=\vec{x}_t} \quad (11)$$

Similarly, the wave function amplitude, A , evolves according to the density continuity equation,

$$\frac{d}{dt}A^2(\vec{x}_t) = -A^2(\vec{x}_t)\nabla^T \cdot \mathbf{G} \cdot \vec{p}_t|_{\vec{x}=\vec{x}_t} \quad (12)$$

From the continuity equation of the probability density, $A^2 = |\psi|^2$, complementary to eq 11, it follows that the probability of finding a particle within the volume element $\delta\vec{x}_t$,

$$\delta\vec{x}_t = dx_{1t} dx_{2t} \dots dx_{N_d t} \quad (13)$$

associated with each trajectory is constant in time.⁶⁶ The volume element $\delta\vec{x}_t$ follows the flow of the QT “fluid” and compresses or expands to compensate changes of the density $A^2(\vec{x}_t)$. This probability

$$w(\vec{x}_t) = A^2(\vec{x}_t)\delta\vec{x}_t, \quad \frac{d}{dt}w(\vec{x}_t) = 0 \quad (14)$$

will be referred to as a trajectory weight, $w(\vec{x}_t)$. Equation 14 allows calculation of expectation values of the position- and momentum-dependent operators, $\hat{\Omega}$, over the QT ensemble without explicit knowledge of the wave function amplitude,

$$\begin{aligned} \langle \hat{\Omega} \rangle_t &= \int \dots \int \psi^*(\vec{x}, t) \hat{\Omega} \psi(\vec{x}, t) \delta\vec{x} \\ &= \int \dots \int |\psi(\vec{x}_t)|^2 \Omega(\vec{x}_t, \vec{p}_t) \delta\vec{x}_t \\ &\approx \sum_k \Omega(\vec{x}_t^{(k)}, \vec{p}_t^{(k)}) w^{(k)} \end{aligned} \quad (15)$$

In eq 15 the multidimensional integration over the coordinate space has been replaced with the summation over the ensemble consisting of a finite number of trajectories (labeled with the superscript k), representing an initial wave function. The trajectory weight, $w^{(k)}$, is a constant-in-time probability of finding a particle within the volume element associated with the k th trajectory,

$$w^{(k)} = A^2(\vec{x}_t^{(k)})\delta\vec{x}_t^{(k)} \quad (16)$$

Equation 15 is used to develop approximations to the quantum potential, which make the QT framework practical for high dimensional systems. The simplest such approximation, i.e., the linearized quantum force implemented in QTES-DFTB, is discussed below (atomic units, specifically $\hbar = 1$ will be used in the remainder of the paper).

Reformulation of the TDSE eq 3 in the trajectory framework elucidates a connection between classical and quantum mechanics but, in general, does not offer computational advantages. Propagation of QTs via eqs 9 requires knowledge of the quantum potential U , defined by eq 10. Efficient evaluation of the quantum potential U is the most challenging part of the QT theory since the direct evaluation of U from the eq 10 requires obtaining values of the function A and its derivatives from the trajectory ensemble. Moreover, the quantum potential U exhibits singularities at the wave function nodes, $A(\vec{x}, t) = 0$, that are associated with the interference effect. In many dimensions, however, the interference is typically quenched⁴⁰ and the quantum potential, which is quadratic in \hbar and inversely proportional to the particle mass, can be interpreted as a correction to the classical motion of the heavy particles. In this regime the dominant QM effects of the nuclear motion may be included via a simple mean-field-type approximation termed the linearized quantum force⁶⁷ (LQF).

The LQF is based on expansion of the components of the nonclassical momentum vector, $\vec{\tau} = A^{-1}\nabla A$, in a basis of linear functions as outlined in Appendix A. The expansion coefficients are determined variationally from the first and second moments of the trajectory distribution, i.e., by the average quantities $\langle 1 \rangle$, $\langle x_n \rangle$, $\langle x_n x_n \rangle$ for $\{n, n'\} = 1 \dots N_d$. Thus, the approximate quantum potential and force are of a mean-field type and the total energy of the QT ensemble is conserved. The LQF approximation is exact for the time-dependent Gaussian wave functions; it describes wave function bifurcation, moderate tunneling (up to 10^{-4}), the ZPE or, more generally, the energy of the wave function localization in space on a time-scale dependent on the anharmonicity. (LQF does not reproduce behavior with interference.) For heavy particles, LQF can be viewed as a correction to the classical force. The scaling of the LQF computation is N_d^3 ; it is performed at every time step and generates the quantum correction for the entire trajectory ensemble. Thus, for all but the simplest analytical classical potentials V , the cost of the quantum correction is a minor addition to the cost of classical dynamics due to evaluations of V and its gradient. QT dynamics with more accurate and more sophisticated approximation to the quantum potential and nonadiabatic extensions are reviewed in ref 58.

2.2. Separation of Quantum and Classical Nuclei. Until now it was assumed that all N_p nuclei and corresponding $N_d = 3N_p$ DoFs are considered quantum. We will now discuss separation of heavy and light nuclei using a time-dependent Hartree product ansatz for the nuclear wave function. For the selected light nuclei the quantum correction on dynamics is included via the quantum potential, determined in practice from the LQF procedure. For the heavy nuclei the quantum potential is significantly smaller and is neglected.

Consider a molecular system comprised of light and heavy particles. Since in the QT formulation contributions to the quantum potential are inversely proportional to particle masses, the quantum force acting on heavy particles can be neglected to yield a mixed quantum/classical dynamics. However, certain care is needed to develop an approach which takes advantage of nuclear mass separation so that it conserves total energy and overcomes the limitation of the traditional Ehrenfest approach.^{59,68,69} Let us divide the full coordinate space into the subspace of dimensionality N_q of coordinates \vec{x} describing $N_q/3$ light, quantum particles and into the subspace \vec{y} of dimensionality $N_c = N_d - N_q$ describing coordinates of $N_c/3$ heavy, nearly classical particles. The volume element in the quantum subspace will be labeled $\delta\vec{x}$ and in the classical subspace $\delta\vec{y}$, defined analogous to eq 13. The subscript of the gradient will denote differentiation with respect to the components of \vec{x} or of \vec{y} . Subscripts q and c will indicate objects associated with the *quantum* and *classical* subspaces, such as amplitudes and phases. The particle masses of the quantum and classical subspaces define matrices \mathbf{G}_q and \mathbf{G}_c as in eq 1.

We assume that the quantum DoFs, \vec{x} , are fast compared to the classical DoFs, \vec{y} . Then the total wave function can be written as a product of the light particle component $\psi_q(\vec{x}, t; \vec{y})$ and the heavy particle component $\psi_c(\vec{y}, t; \vec{x})$; $\psi_q(\vec{x}, t; \vec{y})$ depends on \vec{y} parametrically. Writing both components in terms of real amplitudes and phases the wave function ansatz is

$$\begin{aligned} \psi(\vec{x}, \vec{y}, t) &= \psi_q(\vec{x}, t; \vec{y}) \psi_c(\vec{y}, t) \\ &= A_q(\vec{x}, t; \vec{y}) e^{iS_q(\vec{x}, t; \vec{y})} A_c(\vec{y}, t) e^{iS_c(\vec{y}, t)} \end{aligned} \quad (17)$$

The parametric \vec{y} -dependence of ψ_q and difference in masses means that mass-weighted gradients (element by element) with respect to the classical DoFs are small compared to those for the quantum DoFs,

$$\mathbf{G}_c \cdot \nabla_{\vec{y}} A_q \ll \mathbf{G}_q \cdot \nabla_{\vec{x}} A_q \quad (18)$$

$$\mathbf{G}_c \cdot \nabla_{\vec{y}} S_q \ll \mathbf{G}_q \cdot \nabla_{\vec{x}} S_q \quad (19)$$

Therefore, the terms of the left-hand-side of eqs 18 and 19 can be neglected once the wave function in the form of eq 17 is substituted into the TDSE eq 3. With this simplification, the resulting quantum potential is a sum of light and heavy particle contributions of reduced dimensionality, U_q and U_c , respectively:

$$U = U_q + U_c \quad (20)$$

$$U_q(\vec{x}, t; \vec{y}) = -\frac{\nabla_{\vec{x}}^T \cdot \mathbf{G}_q \cdot \nabla_{\vec{x}} A_q(\vec{x}, t; \vec{y})}{2A_q(\vec{x}, t; \vec{y})} \quad (21)$$

$$U_c(\vec{y}, t) = -\frac{\nabla_{\vec{y}}^T \cdot \mathbf{G}_c \cdot \nabla_{\vec{y}} A_c(\vec{y}, t)}{2A_c(\vec{y}, t)} \quad (22)$$

The ensuing equations of motion for the QTs separate into quantum and classical subspaces when the classical force acting on the coordinates \vec{y} of the classical subspace is averaged with respect to the coordinates \vec{x} of the quantum subspace. Furthermore, neglecting with the quantum potential U_c acting on the heavy particles, the equations of motion for a trajectory $\{\vec{y}_t, \vec{p}_{yt}\}$ in the classical subspace are the following:

$$\begin{aligned} \frac{d\vec{y}_t}{dt} &= \mathbf{G}_c \cdot \vec{p}_{yt}, \\ \frac{d\vec{p}_{yt}}{dt} &= -\int \dots \int \left| \psi_q(\vec{x}, t; \vec{y}_t) \right|^2 \nabla_{\vec{y}} V \Big|_{\vec{y}=\vec{y}_t} \delta \vec{x} \end{aligned} \quad (23)$$

In the quantum subspace the forces acting on the light particle is evaluated at $\vec{y} = \vec{y}_t$, which is consistent with the parametric dependence of ψ_q on \vec{y}_t . The equations of motion for a trajectory $\{\vec{x}_t, \vec{p}_{xt}\}$ of the quantum subspace are the following:

$$\begin{aligned} \frac{d\vec{x}_t}{dt} &= \mathbf{G}_q \cdot \vec{p}_{xt}, \\ \frac{d\vec{p}_{xt}}{dt} &= -\nabla_{\vec{x}} (V(\vec{x}; \vec{y}_t) + U_q(\vec{x}, t; \vec{y}_t)) \Big|_{\vec{x}=\vec{x}_t} \end{aligned} \quad (24)$$

where U_q is given by eq 21 evaluated for $\vec{y} = \vec{y}_t$. Evolution of \vec{y}_t in the classical subspace is governed by the average force from the quantum DoFs for that particular \vec{y}_t . Unlike the conventional Ehrenfest method, a wave function associated with the heavy particles is represented by multiple trajectories, sampling $\psi_c(\vec{y}, 0)$ of eq 17, and the full-dimensional wave function can be recovered at all times (Appendix B). Equations 24 for the quantum DoFs are solved for multiple trajectories \vec{y}_t . The energy is conserved for each “piece”, $\psi_q(\vec{x}, t; \vec{y})$, of the full-dimensional wave function. Further information on the mixed quantum/classical dynamics in terms of discrete trajectories is given in Appendix B.

2.3. Implementation of the Quantum Trajectory Nuclear Dynamics with DFTB. For generality of applications, the PES, i.e., the classical potential V , governing motion of the nuclei is obtained from electronic structure calculations. Each QT describes different configuration of nuclei and requires

independent evaluation of the potential energy and force. This is by far the most expensive part of trajectory simulations. Typically thousands of independent electronic structure evaluations are required for each step of the QT dynamics. Put in perspective, for an ensemble of 1000 trajectories an inexpensive electronic structure evaluation, which takes 3–4 s per single energy and force calculation, will take approximately 1 h for one time step. One hour spent on each time step translates to over 1 year spent on 10 000 time steps of the QT ensemble. Therefore, it is critical to use an inexpensive electronic structure framework and exploit inherent parallelism associated with ensemble of trajectories.

In the current implementation, we use spin-unpolarized SCC-DFTB in conjunction with Fermi–Dirac smearing at an electronic temperature T_{el} .^{54–56,70} The potential energy V for the motion of nuclei in eqs 4 and 9 is given by the Mermin electronic free energy^{71,72}

$$V = E_{el} - T_{el} S_{el} \quad (25)$$

in which E_{el} is the energy obtained by minimization of the electronic wave function using SCC-DFTB at the electronic temperature T_{el} . The second term describes the electronic entropy contribution due to fractional occupancies at nonzero electronic temperature T_{el} .

SCC-DFTB is an approximate DFT method in which only the valence electrons are treated quantum-mechanically while the core electrons and nuclei, referred collectively to as *core ions*, are described via pairwise interatomic potentials

$$E_{el} = \sum_i 2f_i \langle \phi_i | H_0 | \phi_i \rangle + \frac{1}{2} \sum_{\substack{A,B \\ A \neq B}} \gamma^{A,B} \Delta q^A \Delta q^B + \sum_{\substack{A,B \\ \text{atoms}}} E_{rep}^{AB} \quad (26)$$

The quantity f_i is a molecular orbital occupation number that ranges between 0 and 1, given by the Fermi–Dirac distribution; index i runs over all molecular orbitals. The symbols A and B denote different atomic centers. The first right-hand-side term in eq 26 describes interaction of the valence electrons with the core ions. The second term describes electron–electron interaction between the Mulliken charges Δq at different interatomic centers. Symbols Δq^A and $\gamma^{A,B}$ correspond, respectively, to the charge at the center A and to the chemical hardness-based parameter, dependent on the interatomic distance, which describes electron–electron interaction between the centers A and B . In the limit of large interatomic separation between A and B centers, $\gamma^{A,B}$ becomes simply $1/R_{AB}$ following the correct Coulomb asymptotic behavior.⁵⁴

The electronic entropy S_{el} in eq 25 vanishes at zero electronic temperature and the potential energy becomes the ground electronic state. At finite values of the electronic temperature T_{el} , the electronic entropy is given by the following expression, k_B being the Boltzmann constant

$$S_{el} = -2k_B \sum_i [f_i \log(f_i) + (1 - f_i) \log(1 - f_i)] \quad (27)$$

As follows from eq 27, only the orbitals with fractional occupancies near the Fermi level contribute to the electronic entropy, while the contributions of the fully occupied or virtual orbitals are negligible. The potential energy defining motion of the nuclei is, thus, described by the mean field of electrons, which instantaneously equilibrate to the temperature T_{el} . The force derived from the electronic potential energy V , i.e., the “classical” force of the QT formulation, is given by the negative

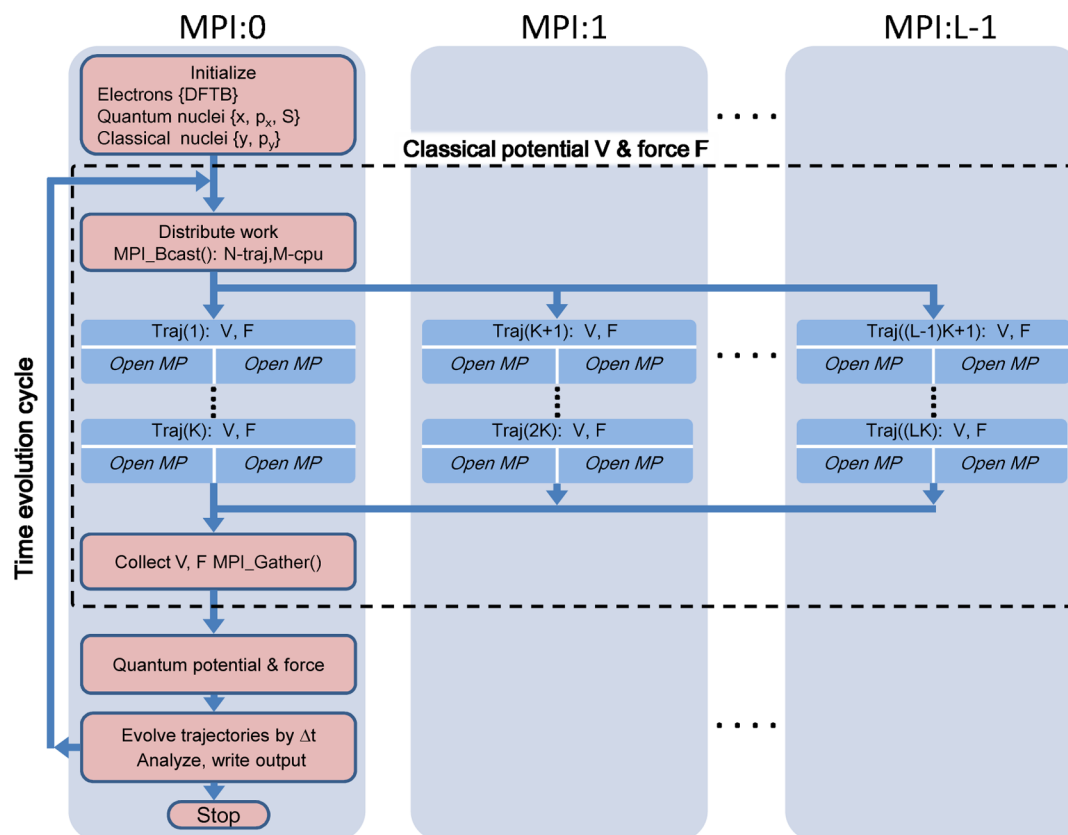


Figure 1. Schematic representation of the parallel implementation of the QTES-DFTB dynamics approach. The electronic structure calculations (inside the dashed box) for all N_{traj} trajectories are distributed across L computing nodes containing multiple cores. (In this work we utilized 12-core nodes of the CRAY XT5.) Each computing node is assigned to a single MPI process and works on the fraction of all trajectories $K = N_{\text{traj}}/L$. Trajectories within each computing node are processed sequentially in a round-robin fashion. On each computing node, evaluation of the DFTB energy and forces is completed in parallel using OpenMP multithreading. All results are gathered on a head node which computes the quantum potential and force and evolves the quantum and classical subsystems.

gradient of V . In principle, the nuclear forces contain the contribution from E_{el} and from S_{el} . Discussion of the forces can be found elsewhere.^{61,73–75}

Our parallel implementation based on open multi-processing (OpenMP) and message passing interface (MPI) is sketched in Figure 1 for L nodes enumerated from 0 to $L - 1$. Here we use the words “node” and “MPI process” interchangeably. The initialization including reading the input (number, type and position of atoms, number of the quantum DoFs, parameters of the initial wavefunction, QT ensemble, and time-propagation) and the DFTB parameter files is performed on the head node. The data are then distributed across the remaining $(L - 1)$ computing nodes. All input/output (IO) operations are performed only once and only on the head node to minimize costly overhead of reading and writing files. Buffered IO is utilized. Next, on the head-node a certain number of trajectories, N_{traj} , representing the initial wavefunction is initialized using random normal deviates⁷⁶ to select their positions $\{\vec{x}^{(k)}, \vec{y}^{(k)}\}$ for $k = 1 \dots N_{\text{traj}}$. The initial momenta $\{\vec{p}_x^{(k)}, \vec{p}_y^{(k)}\}$ and action functions $\{S^{(k)}\}$ are determined by the initial wavefunction evaluated at these positions.

The trajectories are divided into L batches, each one containing no more than N_{traj}/L trajectories. Each batch is assigned to a specific computing node for the entire propagation. Trajectories within a single batch are processed sequentially one after another in a “round-robin” manner. Each computing node is assigned to a single MPI process and can

utilize OpenMP multithreading. The approximate quantum potential U and its gradient are computed on the head-node from the first and second moments of the trajectory positions for the quantum DoFs. To evaluate the classical potential V and its gradient, the trajectory positions $\{\vec{x}^{(k)}, \vec{y}^{(k)}\}$ are passed to their respective computing nodes. Once all DFTB evaluations are finished, the potential energies and gradients are passed back to the head-node, where propagation of the trajectory positions, momenta, and action functions under the influence of the combined potential $V + U$ by a time-step Δt , as well as the calculation of average quantities of interest (probabilities, bond distances, etc.) are performed. The time-propagation cycle is repeated until desired final propagation time is reached.

For a fixed number of the DFTB evaluations, the CPU time is inversely proportional to the number of cores as shown in Figure 2 for a model system of 75 atoms ($\text{C}_{24}\text{H}_{37}\text{FeN}_8\text{O}_5$) discretized with $N_{\text{traj}} = 4800$ QTs. The computational scaling deviates from the ideal case for runs above 1000 cores, since with fewer than 5 trajectories per single computing node load balancing may not be optimal. In other words, since the cost of the SCC-DFTB calculations varies between the trajectories and since average quantities cannot be computed until all single point calculations at a given time step are finished, 10 or more trajectories per core are generally needed to average the numerical cost across the cores.

DFTB scales cubically with the number of valence electrons as seen in Table 1, where the data are given for runs of 4320

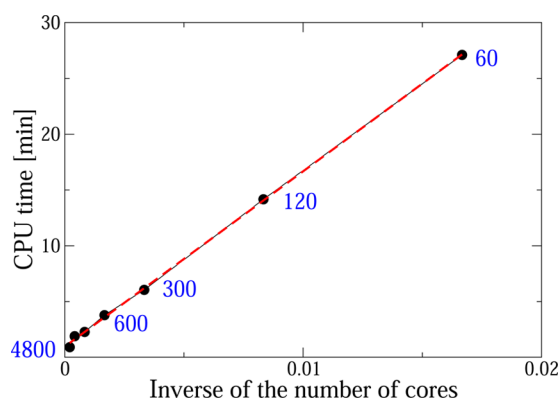


Figure 2. CPU time as a function of the number of cores (also labeled on the plot), for a test system $C_{24}H_{37}FeN_8O_5$ with 75 atoms and 196 basis functions. 4800 trajectories of the QT ensemble were propagated for 25 steps using from 60 to 4800 cores. Single OpenMP thread was used per MPI process. The scaling of numerical cost is inversely proportional to the number of cores. Calculation on a single core would take 26 h. Calculations on 4800 cores took 55 s. This corresponds to average 2.2 s spend on average on a single evaluation of energy and forces.

Table 1. CPU Time Required to Propagate 4320 Trajectories for 1000 Time Steps with 360 Cores on a CRAY XT5^a

structure	$N_{\text{electrons}}$	total time [min]	energy and forces [s]
$C_{24}H_{12} + H$	108	30	0.15
$C_{37}H_{15} + H$	163	77	0.38
$C_{87}H_{23} + H$	371	774	3.87

^aThe last columns shows average time required for a single evaluation of energy and forces. Computational cost is dominated by diagonalization and scales cubically with the system size. All calculations are obtained with single OpenMP thread per MPI process.

trajectories (12 trajectories \times 360 cores); the trajectories were propagated for 1000 time steps. The cubic scaling is due to

diagonalization and other matrix–matrix operations. The numerical cost of computing the quantum potential and force is negligible compared to that of the electronic structure calculations. Overall, the numerical cost of the QT propagation scales linearly with the number of trajectories.

3. SIMULATIONS

We illustrate the QTES-DFTB dynamics approach by examining the adsorption of atomic hydrogen on $C_{37}H_{15}$ (pentabenzocoronene), which is effectively a small “flake” of graphene (see Figure 3). The set of simulations presented in this section is designed to test the validity of the approximations used in QTES method. First, we assess the accuracy of the electronic PES of the QTES code compared to the DFT calculations. Next, we examine the accuracy of LQF benchmarked against exact QM nuclear dynamics in one quantum dimension (the H– $C_{37}H_{15}$ coordinate) coupled to all of the classical DoFs describing the graphene flake. Finally, we present results of three-dimensional QT dynamics for colliding protons and deuterons (all atoms of the graphene flake move, influenced by the classical forces). The effect of the quantum potential U on the dynamics of a QT ensemble is exposed by turning off U , which turns the QT ensemble into a statistical ensemble of independent classical trajectories. Throughout this section for each atom, coordinates (x, y, z) describe its position in the Cartesian system of coordinates.

Isolated $C_{37}H_{15}$ is a flat molecule in xy -plane; the central carbon is located at $(0, 0, 0)$ in Cartesian coordinates. In the dynamics studies presented below, the hydrogen is positioned at zero impact parameter, relative to the central carbon, at $(0, 0, z_0)$ with initial momentum p_0 pointing toward the xy -plane. This is the most reactive collision geometry for the system shown in Figure 3a. The initial separation of H from the plane of $C_{37}H_{15}$ is $z_0 = 6$ bohr along the z -coordinate of the incoming proton. Simulations are performed for a range of collision energies, $E_{\text{coll}} = [0.05, 1.1]$ eV. For higher values of E_{coll} we find that H is fully reflected.

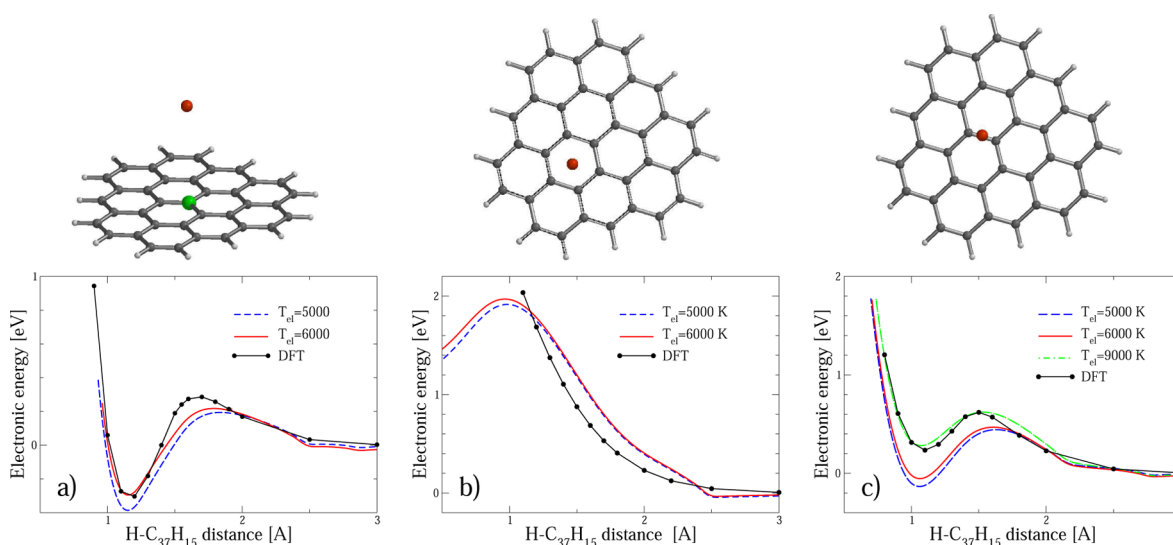


Figure 3. A hydrogen atom (red) colliding with a flat graphene fragment, $C_{37}H_{15}$, at zero impact parameter with respect (a) to the central carbon atom shown in green (lattice-center geometry) or (b) to the hexagon center and to the (c) bond center. The electronic potential energy curves for H + $C_{37}H_{15}$ obtained with DFT and with DFTB, using the G2MS parameter sets, at several electronic temperatures for the (a) lattice-center, (b) hexagon-center, and (c) bond-center geometries.

In this first application of the QTES-DFTB approach, we consider the simplest case and include the quantum force only for the incoming proton. All nuclei of $C_{37}H_{15}$ move according to the classical force averaged over the quantum DoFs; their initial positions sample an initial wave function associated with $C_{37}H_{15}$ as described in section 2.2. The total wave function is a direct product of Gaussian functions in all coordinates. The wave function of the incoming proton is (here coordinates (x, y, z) refer to the proton):

$$\psi_H = \left(\frac{2\alpha}{\pi}\right)^{3/4} e^{-\alpha(z-z_0)^2 + ip_0(z-z_0) - \alpha x^2 - \alpha y^2} \quad (28)$$

where the initial momentum p_0 is in the negative z -direction, $p_0 = -(2mE_{\text{coll}})^{1/2}$; m is the mass of the incoming proton. The width parameter α is taken to be 13 bohr^{-2} , which gives the average quantum potential of 0.096 eV , comparable to the ZPE of a typical CH bond. For $C_{37}H_{15}$ the initial wave function is a product of Gaussian functions of the form given by eq 28, that have zero initial momenta p_0 , centered at the equilibrium position of respective atoms, and have the value of the width parameter α equal to 130 bohr^{-2} in all carbon coordinates.

3.1. Accuracy of the DFTB Potential Energy Surfaces.

Before performing dynamics, we have analyzed the electronic energies obtained from the QTES-DFTB code using the DFT results as a reference. Specifically, we have used the B3LYP/6-31G* level of theory,^{77,78} shown to give adequate description of the electronic structure for the coronene and pyrene molecules.²⁶ The incident hydrogen is an open-shell species and its long-range interaction is dominated by the van der Waals dispersion. The current implementation of the DFTB in the QTES code does not include spin-polarization and dispersion. To mimic the open-shell character of incoming hydrogen interacting with $C_{37}H_{15}$ and to adjust the spin-unpolarized SCC-DFTB potential energy curve to the reference B3LYP/6-31G* curve, we used the Fermi–Dirac smearing characterized by a finite electronic temperature, T_{el} (section 2.3). Use of the finite T_{el} gives certain “multireference” character in the critical for bond formation and breaking region of intermediate H– $C_{37}H_{15}$ distances. At the same time, the finite T_{el} improves convergence of the self-consistent field (SCF) procedure which is beneficial in the context of dynamics. In the course of dynamics, a number of trajectories necessarily will explore spatial regions where SCF convergence is difficult; the finite T_{el} provides a simple “black-box” procedure to alleviate charge “sloshing” and to dampen convergence problems. Due to the large number of individual electronic structure calculations (on the order of millions) required in dynamics, careful analysis and restarting of the SCF procedure are impractical. We note that an alternative approach would be to integrate the time-dependent electronic structure along the trajectories describing nuclear motion.⁶¹

The B3LYP/6-31G* potential energy curves are computed using Q-Chem.⁷⁹ The DFTB and B3LYP energy curves as a function of the distance between H and frozen $C_{37}H_{15}$ are shown in Figure 3 for three positions of incoming hydrogen—lattice-center, bond-center, and hexagon-center. We found that at large separations, the implemented version of the DFTB with the standard MIO parameters⁵⁴ gave qualitatively incorrect energy curves at large separations. To fix this problem in the absence of the spin-polarization and to improve the overall agreement we adjusted the electronic temperature T_{el} and tried new Slater–Koster parameter sets B3 and G2MS developed by

Wang and Irle⁸⁰ based on quantum chemistry data for coronene and pyrene. The G2MS set was found to be the most accurate for $C_{37}H_{15}$. The electronic temperature T_{el} ranging between 1000 and 9000 K has been examined. The best agreement between the DFTB and B3LYP results was found at $T_{\text{el}} = 6000, 5000$, and 9000 K for the lattice-center, hexagon-center, and bond-center geometries, respectively. The lattice center is the most reactive site for hydrogen adsorption (for example, the potential energy curve for hexagon-center is repulsive). Thus, T_{el} of 6000 K was used in all dynamics calculations discussed below.

3.2. One-Dimensional Models for Proton–Graphene Dynamics. The purpose of this section is to analyze and validate approximate QT dynamics. We consider a minimalistic description of the H + $C_{37}H_{15}$ collision occurring in one quantum nuclear DoF, so that the TDSE for this DoF can be solved exactly. The QT dynamics based on the LQF is compared to the exact QM and classical dynamics. Motion of the incoming hydrogen is restricted to the z -coordinate; it is the only quantum coordinate for which the TDSE is solved using the split-operator/fast Fourier transform propagation method.^{81,82} Motion of $C_{37}H_{15}$ is incorporated as described in section 2.2. For the purpose of comparison, the dynamics is performed for a single equilibrium initial configuration of $C_{37}H_{15}$, which makes this description equivalent to the Ehrenfest treatment of the classical DoFs.

The exact QM dynamics for a reactive system governed by a time-dependent potential V is essentially limited to one quantum dimension, because V must be computed at each time-step on a large grid using DFTB. A large spatial grid is required since a wave function of the incoming hydrogen should not be absorbed at the grid boundaries due to averaging of the classical force, $-\nabla V$, acting on a trajectory representing the graphene flake. To enable a comparison of various dynamics methods on the same time-dependent PES, the potential energy curve was parametrized as a function of time and the coordinate z . On the basis of test calculations, for the exact QM dynamics we chose an equidistant grid of 1024 points distributed in the range of $z = [0.0, 50.0] \text{ bohr}$. Time propagations were carried out up to $10\,000 \text{ a.u.}$ with a time step of 4 a.u. The hydrogen was considered adsorbed if its separation from the central carbon was less than 5.5 bohr .

In the QT simulation an ensemble of $N_{\text{traj}} = 4320$ trajectories was evolved on the parametrized time-dependent PES. The initial positions of the trajectories were obtained from a random normal distribution of positions yielding equal trajectory weights, $w^{(k)} = 1/N_{\text{traj}}$. The initial momenta are equal to p_0 of eq 28 according to the definition of QTs. We observed that for this system the quantum potential rapidly decays to zero. Therefore the “zero-order” approximation to the quantum potential has been tested as well. Instead of computing a time-dependent quantum potential, the trajectory momenta at time zero were made equal to the values that trajectories would have after infinitely long evolution in $V = 0$, i. e., the initial momentum of a trajectory initialized at a position $z^{(k)}$ is

$$p(z^{(k)}, 0) = p_0 + 2\alpha(z^{(k)} - z_0) \quad (29)$$

Such spreading of the initial trajectory momenta reproduces the total energy of the wave function.⁸³

The adsorption probability as a function of time for $E_{\text{coll}} = 0.2 \text{ eV}$ calculated with exact QM and with QTs with the LQF on the same parametrized potential is shown in Figure 4. The

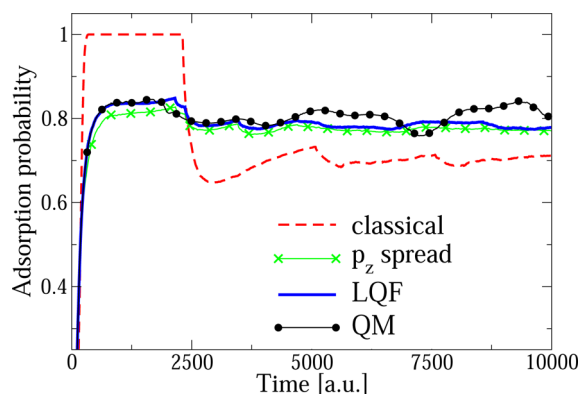


Figure 4. Time-dependent adsorption probability of H on $C_{37}H_{15}$ for the one-dimensional collision model (flexible $C_{37}H_{15}$). The results are obtained from dynamics without the quantum potential, with the momentum spreading, LQF, and from exact QM evolution. Results from the four methods are labeled “classical”, “ p_z spread”, “LQF”, and “QM”, respectively. The time-dependent potential is the same in all calculations.

LQF and exact QM results are in good overall agreement, and are different from the classical, $U = 0$, trajectory dynamics. The dynamics of trajectories with simple spreading of the initial momenta is close to the exact QM results for times longer than 2500 a.u., which indicates that at least in this Ehrenfest-like treatment of carbons the main QM effect comes from localization of the initial wave function, not from the ZPE of the forming CH bond, which is more difficult to capture within the approximate QT approach. This analysis provides some confidence for using the LQF approach for H + $C_{37}H_{15}$ with the on-the-fly potential and in higher dimensionality. Also note that since the momentum-spreading at $t = 0$ mimics the dominant effect of the quantum potential, classical trajectory dynamics with microcanonical or a Wigner-representation sampling may work for this system as well, provided that the quantum/classical mixing scheme is similar to ours. This aspect will be explored in the future.

Adsorption probabilities for various collision energies obtained for one quantum dimension, using the classical potential V computed on-the-fly, with the three methods—exact QM, with and without the quantum potential labeled “QM”, “LQF”, and “classical”, respectively—are shown in Figure 5. The initial wave function is given by eq 28 for $z_0 = 6.0$ bohr. All atoms of $C_{37}H_{15}$ move according to the forces averaged over the quantum DoF. We see that dynamics without the quantum potential produces qualitatively different results compared to the other methods. The total energy of the system is lower than the exact value by $\alpha/(2m)$. The proton wave function essentially maintains its initial localization and the trajectories follow each others’ “footsteps”. For most energies, this dynamics leads to a single probability outcome for all trajectories of the ensemble, i. e., the proton is either fully adsorbed or fully reflected. Both the exact QM and LQF methods yield maximum adsorption of around 70% at $E_{\text{coll}} = 0.2$ eV. The discrepancy between the QM and LQF results come from the fact that the ZPE of the forming CH bond is not captured in this simulation (LQF is essentially zero by the time the hydrogen atom binds to the carbon atom). Nevertheless, the QT results are much closer to the exact QM rather than to the classical dynamics limit.

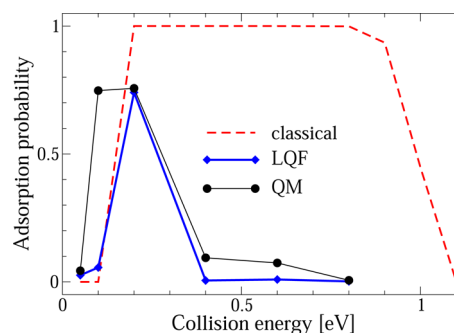


Figure 5. Adsorption probability of H on $C_{37}H_{15}$ obtained from dynamics with and without the quantum potential and with exact QM propagation for the one-dimensional collision model for a range of collision energies. The curves are labeled “LQF”, “classical”, and “QM”, respectively. The target molecule $C_{37}H_{15}$ is flexible; the potential energy V is computed on-the-fly.

To further illustrate the QM behavior of the proton, the adsorption probability and displacement of the central carbon from its original position are shown in Figure 6 as functions of

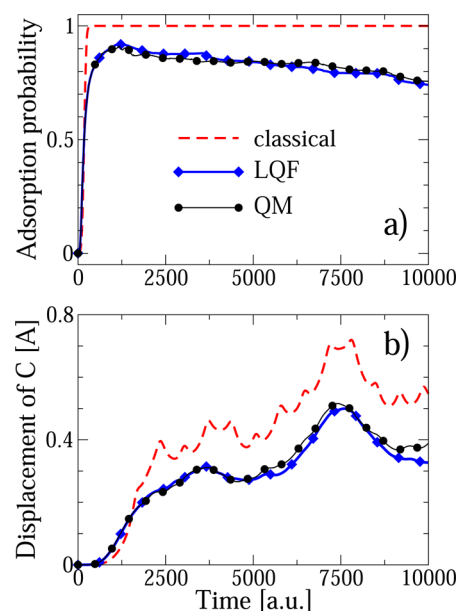


Figure 6. (a) Adsorption probability and (b) position of the central carbon along the collision coordinate as a function of time, obtained from dynamics with and without the quantum potential and with exact QM propagation for the one-dimensional collision model at $E_{\text{coll}} = 0.2$ eV. The legend is the same as in Figure 5.

time for $E_{\text{coll}} = 0.2$ eV. On the upper panel we see that without the quantum potential the incoming proton binds to the target carbon after 500 a.u. with 100% probability and that the collision energy leads to larger displacements of the carbon (as well as vibrations of the entire $C_{37}H_{15}$ molecule). With the QM and LQF methods, a smaller fraction of the trajectories is bonded to the target carbon and a smaller fraction of the collision energy is transferred to $C_{37}H_{15}$ resulting in smaller displacement of the central carbon. Overall, the agreement of the adsorption and carbon displacement between exact QM and approximate QT methods in one quantum dimension is good, which validates the QTES study of higher dimensionality, described below. We estimate that to perform exact QM reactive dynamics with a time-dependent potential in three

dimensions, we would need on the order of 4 million grid points, which is 1000 times more than the number of trajectories required. Thus, we cannot compare exact and approximate dynamics head-to-head. In general, to check the correctness of the approximate QT dynamics we can use more sophisticated (more expensive, not implemented in QTES currently) approximations to the quantum potential and examine the trends in probabilities as has been done for low-dimensional systems. Due to the nonlinear nature of dynamics, convergence to the full QM limit is not systematic (as it would be with the basis size) but in principle the full QM limit is reached if a highly accurate quantum potential is computed.

3.3. Three-Dimensional Proton and Deuteron Dynamics. In this section we discuss the effect of the quantum potential on the motion of incident hydrogen in three dimensions, explore the effect of the isotopic substitution by performing simulations for both hydrogen and deuterium, and go beyond the Ehrenfest treatment by introducing multiple, independent ensembles of QTs. Each ensemble represents a different configuration of atomic positions sampling a wave function of the graphene flake.

For a full-dimensional description of the incoming proton, we include x - and y -coordinates of QTs, representing a three-dimensional initial wave function of eq 28, into the dynamics. The wave function parameters are the same as in section 3.2. As seen in Figure 7, simulations with the three-dimensional (3D)

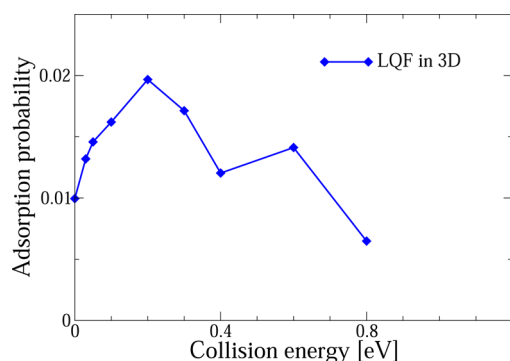


Figure 7. Adsorption probability of H on $C_{37}H_{15}$ obtained with the three-dimensional quantum force acting on the colliding hydrogen. The quantum force is approximated as LQF.

quantum potential show that the maximum adsorption occurs at $E_{\text{coll}} = 0.2$ eV as in the one-dimensional proton dynamics of section 3.2, but the overall probability in 3D case does not exceed 2%. After examining trajectories describing binding of H to $C_{37}H_{15}$, we concluded that in five out of six cases, the colliding proton approaches $C_{37}H_{15}$ at angles of incidence $<10^\circ$. (In the remaining case, this angle was 40° .) Thus, the effect of the lateral components of the quantum force is to spread the wavepacket in xy -plane sending most of the trajectories associated with reflection at higher angles of incidence.

To increase the fraction of adsorbing trajectories which improves sampling, and for closer analogy with the exact QM simulation of section 3.2, we set the lateral components of the quantum force to zero in the analysis below. The quantum potential depends only on the z -coordinate of the colliding hydrogen, but its motion occurs in three Cartesian dimensions. The adsorption probability for a single equilibrium initial configuration of $C_{37}H_{15}$ as a function of the collision energy is very similar to the one-dimensional dynamics as shown in

Figure 8. Without the quantum potential we obtain an adsorption probability above 95% in the range $E_{\text{coll}} = [0.2,$

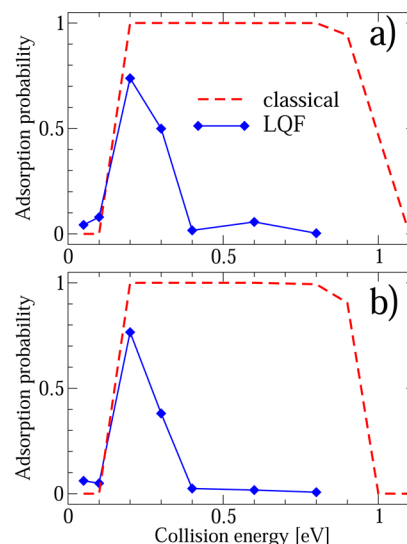


Figure 8. Adsorption probability of H on (a) $C_{37}H_{15}$ and on (b) $C_{87}H_{23}$ obtained with and without the quantum potential, labeled “LQF” and “classical” respectively. The wave function of the colliding proton is three-dimensional, but the quantum force is added only to the z -coordinate, which is the collision direction.

0.9] eV, while with the LQF correction, the adsorption is sharply peaked at 0.2 eV. Time-dependence of the displacement of the central carbon shown in Figure 9, also follows the trend observed in the one-dimensional simulation. In the lower

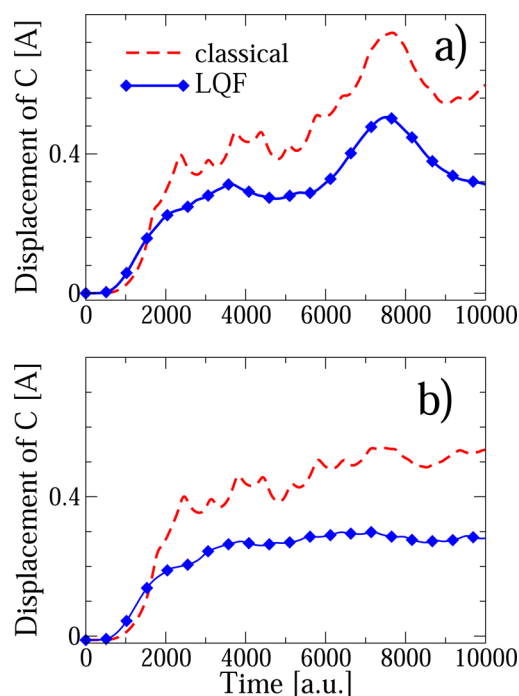


Figure 9. Displacement of the central carbon (the z -coordinate, originally at zero), for (a) $H + C_{37}H_{15}$ and (b) $H + C_{87}H_{23}$. The colliding proton is a three-dimensional quantum particle, the quantum correction is computed only in the z -direction of H. Results of simulations with and without the quantum potential are labeled “LQF” and “classical”, respectively.

panels of both Figures 8 and 9, we show results of simulations for a larger graphene flake, $C_{87}H_{23}$. The overall behavior of the adsorption probability as a function of E_{coll} and of the carbon displacements as a function of time, is similar to that of $C_{37}H_{15}$, although the dynamics of the central carbon is smoother. Therefore, we conclude that $C_{37}H_{15}$ examined in greater detail is sufficiently large to argue that the main QM effects come from the localization of the initial wave function.

Finally, going beyond the Ehrenfest treatment of $C_{37}H_{15}$, we introduce sampling of atoms of the graphene flake positions as described in section 2.2. The adsorption probability is averaged over multiple ensembles of the quantum trajectories. These ensembles are independent of each other; their number, which was <15 in this simulation, depends on the acceptable level of convergence of adsorption probability. To explore the effect of the isotopic substitution, the QT dynamics was performed for both hydrogen and deuterium. The results are shown in Figure 10. For the hydrogen, the LQF dynamics gives a lower

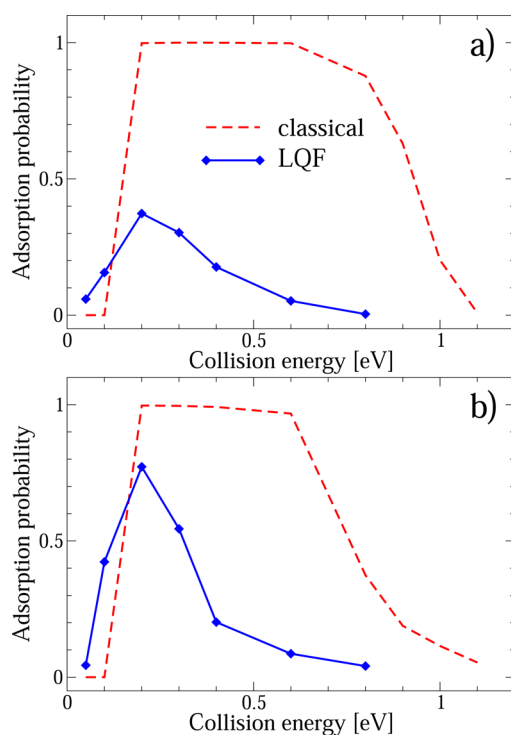


Figure 10. Adsorption probability of H on $C_{37}H_{15}$ obtained with multiple ensembles, representing the initial wave function of $C_{37}H_{15}$, as described in section 2.2. Converged probabilities are obtained with 11 ensembles for the hydrogen and with 14 ensembles for the deuterium shown on panels a and b, respectively. The legend is the same as in Figure 9

maximum adsorption of 40%, due to contributions from initial configurations with nonoptimal bonding, as well as more gradual changes between low and high probabilities. Simulations without the quantum potential, still show a maximum of 100%, although over a shorter range of collisions energies, $E_{\text{coll}} = [0.2, 0.6]$ eV. Results for deuterium exhibit the same overall trends. The higher adsorption probability can be explained by longer interaction times for the colliding particle with the graphene flake which allows for more efficient transfer of the collision energy to the graphene flake. Overall, inclusion of a quantum treatment for the incident proton/deuteron leads to significantly increased adsorption of deuterium compared to

hydrogen. At the collision energy of 0.2 eV, the ratio of adsorption probabilities is close to 3, which is not observed in the classical simulations. This observation can be tested experimentally and could potentially find an application in selective binding of deuterium.

4. CONCLUSIONS

We have described a direct quantum molecular dynamics approach, QTES-DFTB, combining the approximate Bohmian or quantum trajectory (QT) representation of time-dependent nuclear wave functions with the on-the-fly electronic structure (ES) calculations at the density functional tight binding (DFTB) level. Several models for one-dimensional and three-dimensional hydrogen have been tested. As the first application of the QTES-DFTB dynamics, we have examined adsorption of atomic hydrogen on $C_{37}H_{15}$ at collision energies below 1.0 eV. Within the QT framework, the QM effects on the moving nuclei stem from the quantum potential and quantum force entering the equations of motion for the trajectories alongside the electronic potential energy and the corresponding force. The simplest physically meaningful mean-field approximation to the quantum potential generates the linearized quantum force (LQF). The LQF is exact for a time-dependent Gaussian wave function, accurately describes its spreading/contraction behavior, but at the same time allows for wave function bifurcation into distinct reaction channels. The computation of LQF is a negligible overhead compared to the computational cost of the external “classical” potential, i. e., the DFTB calculations.

In the current implementation different trajectories are distributed across multiple computing nodes using MPI, while the single point DFTB calculations are accomplished using OpenMP within a computing node. Information from the entire trajectory ensemble representing the nuclear wave function—positions, momenta, action functions—are collected on a head-node to compute the quantum correction for the dynamics and the quantities of interest, such as expectation values, bond distances, etc. We have demonstrated that this parallel implementation, which minimizes data passing between the computing nodes, scales linearly (for a fixed size problem) up to 1000 MPI processes. A typical simulation (50–100 atoms, 5000 trajectories, 1000 time steps, 300 MPI processes) takes just a few hours on the CRAY XT5, specifically on Kraken of The National Institute for Computational Sciences. For the dynamics studies of H colliding with $C_{37}H_{15}$ reported here, typical runs of 4320 trajectories on 360 cores propagated for 1000 time-steps with the quantum correction for one atom took 77 min of wall-clock time. In test runs with two quantum nuclei the CPU time increased by 14%.

The quantum correction to dynamics is applied to selected nuclei to reduce computational cost and to improve accuracy of the LQF. Our mixed quantum/classical description of light and heavy (or quantum and nearly classical) nuclei is developed within the QT framework. The quantum force acts on selected DoFs describing particles, for which the quantum effects are expected to be significant. Motion of the heavy particles is influenced by the classical potential (coming from DFTB) averaged over the quantum DoFs. In the QT-based mixed quantum/classical dynamics, unlike in the Ehrenfest description, the wave function of heavy particles is represented by multiple trajectories in the classical DoFs and a full-dimensional wave function can be reconstructed at all times. The mixed quantum/classical Bohmian dynamics strictly conserves total

energy of trajectory ensembles in the quantum DoFs, guided by the trajectories in the classical DoFs. The trajectories in the classical DoFs do not interact, which makes it convenient to test convergence with respect to the number of configurations sampling an initial wave function of the nearly classical DoFs. As a note of caution, the QT ensembles guided by noninteracting trajectories in the classical DoFs, do not exchange energy which is a limitation of accuracy of the approach. The “noninteraction” constraint will be relaxed in a future implementation.⁸⁴

In the application to adsorption of atomic hydrogen on $C_{37}H_{15}$, described in section 3, the LQF correction has been made for the colliding hydrogen. We have found that the dominant quantum effect comes from the distribution of the translational energy components in a wavepacket describing the proton. Neglecting the quantum correction in the collision DoF leads to noticeable differences in the dynamics of the graphene flake, $C_{37}H_{15}$, resulting in overestimation of adsorption. This conclusion is supported by comparison of approximate QT and exact QM dynamics in one quantum DoF governed by the same time-dependent motion of the $C_{37}H_{15}$ potential. Applications of the QTES-DFTB dynamics to systems with more quantum nuclei are in progress.

In future developments we will focus on including spin-polarization into the DFTB component and on going beyond the LQF approximation in the dynamics component of QTES-DFTB. Target applications include study of nanomaterials with the focus on the quantum nuclear effect and coupling with electronic structure.

■ APPENDIX A: LINEARIZED QUANTUM FORCE APPROXIMATION

The quantum potential of eq 10 can be equivalently written in terms of the *nonclassical* component of the momentum operator, a vector denoted \vec{r}

$$\vec{r} = \frac{\nabla A}{A} \quad (30)$$

$$U = -\frac{1}{2}(\vec{r}^T \cdot \mathbf{G} \cdot \vec{r} + \nabla^T \cdot \mathbf{G} \cdot \vec{r}) \quad (31)$$

For a Gaussian wavefunction components of the nonclassical momentum vector are time-dependent linear functions of all coordinates. As a simple approximation, an expansion of \vec{r} in terms of the linear functions can be defined for any wavefunction. Using \vec{f} to denote a vector of basis functions

$$\vec{f}^T = [\vec{x}, 1] = [x_1, x_2, \dots, x_{N_d}, 1] \quad (32)$$

components of the vector \vec{r} , can be approximated as

$$r_n \approx \vec{f}^T \cdot \vec{c}_n, \quad n = 1 \dots N_d \quad (33)$$

Vectors \vec{c}_n are of dimensionality $N_d + 1$. Each \vec{c}_n vector out of all N_d vectors describes expansion coefficients of the n th component of \vec{r} . The approximate \vec{r} in the form of eq 33 defines an analytic quadratic quantum potential U according to eq 31 and corresponding to a linearized quantum force (LQF), $\vec{F}_{qm} = -\nabla U$.

Arranging the expansion coefficients as columns of a matrix $\mathbf{C} = [\vec{c}_1, \vec{c}_2, \dots, \vec{c}_{N_d}]$, these coefficients are determined by a least squares fit procedure resulting in a linear matrix equation,⁶⁷

$$\mathbf{MC} = \mathbf{B} \quad (34)$$

In eq 34, the elements of the overlap matrix \mathbf{M} and of the right-hand-side matrix \mathbf{B} are

$$M_{ij} = \langle f_i f_j \rangle, \quad B_{ij} = -\frac{\langle 1 \rangle}{2} \delta_{ij} \quad (35)$$

The averages in eq 35 are computed according to eq 15; δ_{ij} is the Kronecker delta. The procedure defined by eqs 33–35 is equivalent to the variational determination of U given by eq 31 within the basis representation of \vec{r} .⁶⁷ Therefore, the method conserves total energy.

Matrix \mathbf{C} , solving the system of linear equations of eq 34, defines the nonclassical momentum components of the vector \vec{r} according to eq 33. Within the LQF approximation these components are first-order polynomials of N_d coordinates,

$$r_n = \sum_{j=1}^{N_d} c_{jn} x_j + c_{(N_d+1)n} \quad (36)$$

where variables from x_1 to x_{N_d} are instantaneous positions of QTs. The resulting linear functions \vec{r} from the fit, inserted into eq 31, define an analytical quantum potential and its gradient. For the special case of r_n being a linear function of coordinates, the second term in eq 31 is proportional to the sum of the diagonal elements of \mathbf{C} , and though it depends on time, it does not contribute to the quantum force. Thus the linear form of r_n yields the linear quantum force, which gives exact quantum dynamics, including spreading and localization, of a Gaussian wavefunction evolving in a quadratic potential, and defines the approximate LQF dynamics for anharmonic potentials.

An obvious limitation of the LQF approximation is its mean-field character, which introduces nonphysical interaction between spatially distinct parts of a wavefunction. For example, in reactive scattering the LQF approaches zero as the transmitted and reflected parts of a wavefunction separate. For high-dimensional systems consisting of light and heavy particles this shortcoming can be alleviated, since wavefunctions often decohere in the classical DoFs: the LQF can be included selectively into the quantum DoFs^{57,84} and computed from averaging over similar configurations of the classical particles. This strategy will give more accurate LQF at a reduced numerical cost. One such approach, a mixed quantum/classical Bohmian dynamics⁵⁷ is implemented in the QTES-DFTB code.

■ APPENDIX B: IMPLEMENTATION OF MIXED QUANTUM/CLASSICAL TRAJECTORY DYNAMICS

To compute average quantities over the full-dimensional wavefunction in the form of eq 17, the trajectory weights in the quantum and classical subspaces may be used. If the fast component, $\psi_q(\vec{x}, t; \vec{y})$, is normalized to 1 for each \vec{y}_t of the classical subspace, then the trajectory weights w_q and w_c are conserved separately in the quantum and classical subspaces,

$$w_q = A_q^2(\vec{x}_t; \vec{y}_t) \delta \vec{x}_t, \quad w_c = A_c^2(\vec{y}_t) \delta \vec{y}_t \quad (37)$$

The phase of the total N_d -dimensional wavefunction at the quantum and classical trajectory positions,

$$\psi(\vec{x}_t, \vec{y}_t) = A_q(\vec{x}_t; \vec{y}_t) A_c(\vec{y}_t) \exp(iS(\vec{x}_t, \vec{y}_t)) \quad (38)$$

becomes

$$S(\vec{x}_t, \vec{y}_t) = S(\vec{x}_0, \vec{y}_0) + \int_0^t \left(\frac{1}{2} (\vec{p}_{y\tau}^T \cdot \mathbf{G}_c \cdot \vec{p}_{y\tau} + \vec{p}_{x\tau}^T \cdot \mathbf{G}_q \cdot \vec{p}_{x\tau}) - V(\vec{x}_\tau, \vec{y}_\tau) - U_q(\vec{x}_\tau; \vec{y}_\tau) \right) d\tau \quad (39)$$

The energy, $E(\vec{y}_t)$, is conserved for each $\psi_q(\vec{x}, t; \vec{y})$

$$\begin{aligned} E(\vec{y}) &= \langle \hat{H} \rangle_{\vec{x}} \\ &= \int \dots \int |\psi(\vec{x}, \vec{y}_t)|^2 \left(\frac{1}{2} (\vec{p}_x^T \cdot \mathbf{G}_q \cdot \vec{p}_x + \vec{p}_{y_t}^T \cdot \mathbf{G}_c \cdot \vec{p}_{y_t}) + V(\vec{x}, \vec{y}_t) + U_q(\vec{x}, t; \vec{y}_t) \right) d\vec{x} \end{aligned} \quad (40)$$

Discretizing the initial wavefunction in the classical DoFs via trajectories $\{\vec{y}^j\}$ (with the superscript j) and furthermore for each j discretizing in the quantum subspace in terms of the quantum trajectories (with the superscript $k(j)$), the expectation values are

$$\langle \langle \hat{\Omega} \rangle_{\vec{x}} \rangle_{\vec{y}} = \sum_{j,k(j)} w_c^j w_q^{k(j)} \Omega(\vec{x}^{k(j)}, \vec{y}^j) \quad (41)$$

For numerical efficiency and scalability the quantum force acting in \vec{x} , i. e. only in the quantum DoFs, is computed within the LQF approximation of Appendix A.

For simplicity of presentation, consider a separable initial wavefunction,

$$\psi(\vec{x}, \vec{y}, 0) = \psi_q(\vec{x}, 0; \vec{y}) \psi_c(\vec{y}, 0)$$

where ψ_c is a Gaussian in N_c dimensions,

$$\psi_c(\vec{y}, 0) = \left(\frac{2\beta}{\pi} \right)^{N_c/4} \exp(-\beta(\vec{y} - \vec{Y}_0)^2 + i\vec{p}_{y0}(\vec{y} - \vec{Y}_0)) \quad (42)$$

Vectors \vec{p}_{y0} and \vec{Y}_0 define the initial phase and position of a wavefunction, β is a positive parameter or, more generally, a symmetric positive-definite matrix of parameters, defining localization or “width” of the Gaussian. To evolve the heavy particle, i.e. the nearly-classical component of the wavefunction, $\psi_c(\vec{y}, 0)$ is represented in terms of trajectories with initial positions \vec{y}_0^j . The weight of the trajectory \vec{y}_t^j is its contribution to the expectation values, which is a constant at all times

$$w_c^j = |\psi_c(\vec{y}_0^j)|^2 \delta \vec{y}_0^j$$

According to the QT definition of eq 6, the initial trajectory momenta is set to $\vec{p}_y^j(t=0) = \vec{p}_{y0}$. In our experience however,⁵⁷ since we neglect with the quantum potential in the classical DoFs, we find it useful to *adjust* the initial momenta so that the energy of $\psi_c(\vec{y}, 0)$ has exact QM value. Thus, the initial trajectory momenta are set as

$$\vec{p}_y^j(t=0) = \vec{p}_{y0} + 2\beta(\vec{y}_0^j - \vec{Y}_0) \quad (43)$$

This adjustment gives extra energy to the trajectories at the leading part of the wavepacket, $\vec{y}_0^j > \vec{y}_0$, and reduces energy for the trajectories at the trailing part of a wavepacket, $\vec{y}_0^j < \vec{y}_0$. This heuristic modification of initial \vec{p}_y^j gives correct energy at infinite time for a QT describing evolution of a Gaussian in free space. According to the mixed quantum/classical dynamics of section 2.2 trajectories $\{\vec{y}_t^j, \vec{p}_{y_t}^j\}$ in the classical subspace evolve independently of each other.

Next, for *each* \vec{y}_0^j the light particle wavefunction $\psi_q(\vec{x}, 0; \vec{y}_0^j)$ of the quantum subspace is discretized in terms of the QT ensemble. For the initial trajectory positions \vec{x}_0^k (suppressing j in $k(j)$ subscripts) the corresponding momenta are

$$\vec{p}_x^k(t=0) = \nabla_{\vec{x}} S_q(\vec{x}, 0; \vec{y}_0^j) \Big|_{\vec{x}=\vec{x}_0^k}$$

The QT weight, or contribution of $\psi_q(\vec{x}, t; \vec{y}_t^j)$ to the expectation values, is

$$w_q^k = |\psi_q(\vec{x}_0^k; \vec{y}_0^j)|^2 \delta \vec{x}_0^k$$

Trajectories $\{\vec{x}_t^k\}$ and $\{\vec{y}_t^j\}$ evolve in their respective quantum and classical subspaces according to eqs 24 and 23.

In the numerical implementation the sampling of trajectory positions (\vec{x}, \vec{y}) can be performed in full dimensionality using random or quasi-random number generator and normal distribution of sampling points.⁷⁶ For a Gaussian initial wavefunction the normal sampling (or its equivalent for other initial wavefunctions) is advantageous in high dimensionality.

Once a set of N_{traj} (thousands) points $\{\vec{x}_0^n, \vec{y}_0^n\}$ for $n = 1 \dots N_{\text{traj}}$ is constructed, then an ensemble of N_{traj} QTs in the quantum \vec{x} -subspace $\{\vec{x}_0^k\}$, $k = 1 \dots N_{\text{traj}}$ coupled to the first trajectory in the classical \vec{y} -subspace with initial condition \vec{y}_0^j for $j = 1$ is evolved. Evolution of the first QT ensemble is followed by the second ensemble initialized by the same initial QT positions $\{\vec{x}_0^k\}$, $k = 1 \dots N_{\text{traj}}$ and $\vec{y} = \vec{y}_0^j$ for $j = 2$ and so on. The quantum trajectory ensembles, their number N_{ens} (dozens or hundreds) typically much smaller than N_{traj} , are evolved sequentially until convergence of the target quantity is reached with respect to N_{ens} .

For an implementation that is efficient in many dimensions, the evolution of each QT ensemble can be accomplished using the LQF of Appendix A, which is a global mean-field approximation to the quantum potential and force. If the number of quantum DoFs is limited to 1–3, then as in refs 47 and 59 a conventional time-dependent method can be employed to evolve $\psi_q(\vec{x}, t; \vec{y}_t)$,

$$\left(-\frac{1}{2} \nabla_{\vec{x}}^T \cdot \mathbf{G}_q \cdot \nabla_{\vec{x}} + V(\vec{x}, \vec{y}_t) \right) \psi_q(\vec{x}, t; \vec{y}_t) = i \frac{\partial}{\partial t} \psi_q(\vec{x}, t; \vec{y}_t) \quad (44)$$

coupled with evolution of y_t according to eq 23. The total wavefunction in this case becomes

$$\psi(\vec{x}, \vec{y}_t) = \psi_q(\vec{x}, t; \vec{y}_t) \exp\left(\frac{i}{2} \int_0^t \vec{p}_{y\tau}^T \cdot \mathbf{G}_c \cdot \vec{p}_{y\tau} d\tau \right) A_c(\vec{y}_t) \quad (45)$$

■ ASSOCIATED CONTENT

Supporting Information

Two animations show a hydrogen atom colliding with $\text{C}_{37}\text{H}_{15}$ simulated with the QTES- DFTB method. The collision energy is 0.4 eV. The colliding hydrogen is treated as a quantum particle and its wavefunction is represented with an ensemble of 10000 trajectories shown as a white swarm. The initial positions of carbons, shown in blue, are displaced from the equilibrium. In the simulation without the quantum correction on dynamics the entire ensemble becomes trapped near $\text{C}_{37}\text{H}_{15}$. Some of the kinetic energy of hydrogen is transferred to the vibrations of $\text{C}_{37}\text{H}_{15}$; the adsorption probability of 100%. When the approximate quantum correction is included, the trajectory ensemble bifurcates and only 22% of the trajectories become

trapped near $C_{37}H_{15}$. The classical force acting on $C_{37}H_{15}$ is found by averaging over the trajectory ensemble, thus dynamics of $C_{37}H_{15}$ in two simulations differs. This material is available free of charge via the Internet at <http://pubs.acs.org>.

AUTHOR INFORMATION

Corresponding Authors

*E-mail: garashchuk@sc.edu.

*E-mail: jjakowski@utk.edu.

Notes

The authors declare no competing financial interest.

ACKNOWLEDGMENTS

Acknowledgment is made to the donors of the American Chemical Society Petroleum Research Fund for partial support of this research. This material is based upon work partially supported by the National Science Foundation under Grants No. CHE-1056188 (S.G.) and ARRA-NSF-EPS-0919436 (J.J.). B.G.S. acknowledges support from the Center for Nanophase Materials Sciences, which is sponsored at Oak Ridge National Laboratory by the Scientific User Facilities Division, office of Basic Energy Sciences, U.S. Department of Energy (DOE). Some mathematical aspects of the work were supported by the Mathematical Multifaceted Integrated Centers within the Applied Mathematics activity of the U.S. DOE Advanced Scientific Computing Research program. XSEDE allocation TG-DMR110037 time on Kraken at the National Institute for Computational Sciences and use of USC HPC cluster funded by the National Science Foundation under Grant No. CHE-1048629 are also acknowledged.

REFERENCES

- (1) Wang, Q.; Challa, S. R.; Sholl, D. S.; Johnson, J. K. *Phys. Rev. Lett.* **1999**, *82*, 956–959.
- (2) Niimura, S.; Fujimori, T.; Minami, D.; Hattori, Y.; Abrams, L.; Corbin, D.; Hata, K.; Kaneko, K. *J. Am. Chem. Soc.* **2012**, *134*, 18483–18486.
- (3) FitzGerald, S. A.; Pierce, C. J.; Rowsell, J. L. C.; Bloch, E. D.; Mason, J. A. *J. Am. Chem. Soc.* **2013**, *135*, 9458–9464.
- (4) Martinez-Mesa, A.; Zhechkov, L.; Yurchenko, S. N.; Heine, T.; Seifert, G.; Rubayo-Soneira, J. *J. Phys. Chem. C* **2012**, *116*, 19543–19553.
- (5) Hayes, R. L.; Paddison, S. J.; Tuckerman, M. E. *J. Phys. Chem. B* **2009**, *113*, 16574–16589.
- (6) Hayes, R. L.; Paddison, S. J.; Tuckerman, M. E. *J. Phys. Chem. A* **2011**, *115*, 6112–6124.
- (7) Dellago, C.; Naor, M. M.; Hummer, G. *Phys. Rev. Lett.* **2003**, *90*, 105902.
- (8) Dimitrakakis, G. K.; Tylanakis, E.; Froudakis, G. E. *Nano Lett.* **2008**, *8*, 3166–3170.
- (9) Krstic, P. S.; Allain, J. P.; Taylor, C. N.; Dadras, J.; Maeda, S.; Morokuma, K.; Jakowski, J.; Allouche, A.; Skinner, C. H. *Phys. Rev. Lett.* **2013**, *110*, 105001.
- (10) Ito, A.; Wang, Y.; Irle, S.; Morokuma, K.; Nakamura, H. Molecular dynamics simulation of hydrogen atom sputtering on the surface of graphite with defect and edge. *Proceedings of the 18th International Conference on Plasma-Surface Interactions in Controlled Fusion Device*, Toledo, Castilla-La Mancha, Spain, May 26–30, 2008; Journal of Nuclear Materials, 2009; pp 183–187.
- (11) Schedin, F.; Geim, A. K.; Morozov, S. V.; Hill, E. W.; Blake, P.; Katsnelson, M. I.; Novoselov, K. S. *Nat. Mater.* **2007**, *6*, 652–655.
- (12) Ehemann, R. C.; Krstic, P. S.; Dadras, J.; Kent, P. R. C.; Jakowski, J. *Nanoscale Res. Lett.* **2012**, *7*, 1–14.
- (13) Voth, G. A. *Acc. Chem. Res.* **2006**, *39*, 143–150.
- (14) Hummer, G.; Rasaiah, J. C.; Noworyta, J. P. *Nature* **2001**, *414*, 188–190.
- (15) Garberoglio, G. *Eur. Phys. J. D* **2009**, *51*, 185–191.
- (16) Garberoglio, G. *J. Chem. Phys.* **2008**, *128*, 134109.
- (17) Beenakker, J.; Borman, V.; Krylov, S. *Chem. Phys. Lett.* **1995**, *232*, 379–382.
- (18) Hathorn, B. C.; Sumpter, B. G.; Noid, D. W. *Phys. Rev. A* **2001**, *64*, 022903.
- (19) Manzhos, S. *Aust. J. Chem.* **2013**, *66*, 1021–1028.
- (20) Shao, M.; Keum, J.; Xiao, K.; Hong, K.; Chen, J.; He, Y.; Chen, W.; Browning, J.; Jakowski, J.; Sumpter, B. G.; Ilia, N.; Ivanov, I. N.; Ma, Y.; Rouleau, C. M.; Geohegan, D. B. *Nature Comm.* (submitted).
- (21) Ito, A.; Nakamura, H.; Takayama, A. *J. Phys. Soc. Jpn.* **2008**, *77*, 114602.
- (22) Sakong, S.; Kratzer, P. *J. Chem. Phys.* **2010**, *133*, 054505.
- (23) Spirko, V.; Rubes, M.; Bludsky, O. *J. Chem. Phys.* **2010**, *132*, 194708.
- (24) Casolo, S.; Livvik, O. M.; Martinazzo, R.; Tantardini, G. F. *J. Chem. Phys.* **2009**, *130*, 054704.
- (25) Haberer, D.; Giusca, C. E.; Wang, Y.; Sachdev, H.; Fedorov, A. V.; Farjam, M.; Jafari, S. A.; Vyalikh, D. V.; Usachov, D.; Liu, X.; Treske, U.; Grobosch, M.; Vilkov, O.; Adamchuk, V. K.; Irle, S.; et al. *Adv. Mater.* **2011**, *23*, 4497.
- (26) Wang, Y.; Qian, H.-J.; Morokuma, K.; Irle, S. *J. Phys. Chem. A* **2012**, *116*, 7154–7160.
- (27) Karplus, M.; Sharma, R. D.; Porter, R. N. *J. Chem. Phys.* **1964**, *40*, 2033.
- (28) Zhu, X.; Lopes, P.; MacKerell, A. D. *Wiley interdis. rev.—Comput. Mol. Sci.* **2012**, *2*, 167–185.
- (29) Cha, Y.; Murray, C. J.; Klinman, J. P. *Science* **1989**, *243*, 1325–1330.
- (30) Dekker, C.; Ratner, M. A. *Phys. World* **2001**, *14*, 29–33.
- (31) Knapp, M. J.; Klinman, J. P. *Eur. J. Biochem.* **2002**, *269*, 3113–3121.
- (32) Killelea, D. R.; Campbell, V. L.; Shuman, N. S.; Utz, A. L. *Science* **2008**, *319*, 790–793.
- (33) Zhang, W.; Kawamata, H.; Liu, K. *Science* **2009**, *325*, 303–306.
- (34) Han, Y.-C.; Bowman, J. M. *Chem. Phys. Lett.* **2013**, *556*, 39–43.
- (35) Czako, G.; Kaledin, A. L.; Bowman, J. M. *J. Chem. Phys.* **2010**, *132*, 164103.
- (36) Czako, G.; Kaledin, A. L.; Bowman, J. M. *Chem. Phys. Lett.* **2010**, *500*, 217–222.
- (37) Light, J. C.; Carrington, T., Jr. *Adv. Chem. Phys.* **2000**, *114*, 263–310.
- (38) Herman, M. F.; Kluk, E. *Chem. Phys.* **1984**, *91*, 27.
- (39) Kay, K. G. *J. Chem. Phys.* **1994**, *100*, 4377–4392.
- (40) Miller, W. H. *J. Phys. Chem. A* **2001**, *105*, 2942–2955.
- (41) Ben-Nun, M.; Quenneville, J.; Martinez, T. J. *J. Chem. Phys.* **2001**, *104*, 5161–5175.
- (42) Kim, S. Y.; Hammes-Schiffer, S. *J. Chem. Phys.* **2006**, *124*, 244102.
- (43) Prezhdo, O.; Kisil, V. *Phys. Rev. A* **1997**, *56*, 162–175.
- (44) Hone, T. D.; Izvekov, S.; Voth, G. A. *J. Chem. Phys.* **2005**, *122*, 054105.
- (45) Gao, J.; Truhlar, D. G. *Annu. Rev. Phys. Chem.* **2002**, *53*, 467–505.
- (46) Náray-Szabó, G.; Warshel, A., Eds. *Computational approaches to biochemical reactivity; Understanding chemical reactivity*; Kluwer Academic Publishers, 1997; Vol. 19.
- (47) Gindensperger, E.; Meier, C.; Beswick, J. A. *J. Chem. Phys.* **2000**, *113*, 9369–9372.
- (48) Craig, I. R.; Manolopoulos, D. E. *J. Chem. Phys.* **2005**, *122*, 084106.
- (49) Habershon, S.; Manolopoulos, D. E. *J. Chem. Phys.* **2009**, *131*, 244302.
- (50) Tuckerman, M. E.; Berne, B. J.; Martyna, G. J.; Klein, M. L. *J. Chem. Phys.* **1993**, *99*, 2796–2808.
- (51) Hetenyi, B.; Rabani, E.; Berne, B. J. *J. Chem. Phys.* **1999**, *110*, 6143–6153.

- (52) Geneste, G.; Dammak, H.; Hayoun, M.; Thiercelin, M. *Phys. Rev. B* **2013**, *87*, 014113.
- (53) Stuart, S. J.; Nugawela, D.; Hadri, B.; Jakowski, J.; Krstic, P.; Garashchuk, S.; Irle, S. Optimization of Density Functional Tight-Binding and Classical Reactive Molecular Dynamics for High-Throughput Simulations of Carbon Materials. *Conference proceedings of XSEDE12*, Chicago, July 16–19, 2012.
- (54) Elstner, M.; Porezag, D.; Jungnickel, G.; Elsner, J.; Haugk, M.; Frauenheim, T.; Suhai, S.; Seifert, G. *Phys. Rev. B* **1998**, *58*, 7260–7268.
- (55) Porezag, D.; Frauenheim, T.; Käübler, T.; Seifert, G.; Kaschner, R. *Phys. Rev. B* **1995**, *51*, 12947.
- (56) Zheng, G.; Lundberg, M.; Jakowski, J.; Vreven, T.; Frisch, M. J.; Morokuma, K. *Int. J. Quantum Chem.* **2009**, *109*, 1841–1854.
- (57) Garashchuk, S.; Volkov, M. V. *Mol. Phys.* **2012**, *110*, 985–993.
- (58) Garashchuk, S.; Rassolov, V.; Prezhdo, O. *Reviews in Computational Chemistry*; Wiley, 2011; Vol. 27, Chapter Semiclassical Bohmian dynamics, pp 111–210.
- (59) Prezhdo, O. V.; Brooksby, C. *Phys. Rev. Lett.* **2001**, *86*, 3215–3219.
- (60) Ohrn, N. Y. J. *Phys. Chem. A* **2001**, *105*, 2660–2667.
- (61) Jakowski, J.; Morokuma, K. *J. Chem. Phys.* **2009**, *130*, No. 224106.
- (62) Iyengar, S. S.; Jakowski, J. *J. Chem. Phys.* **2005**, 122.
- (63) Rassolov, V. A.; Garashchuk, S.; Schatz, G. C. *J. Phys. Chem. A* **2006**, *110*, 5530–5536.
- (64) Madelung, E. Z. *Phys.* **1927**, *40*, 322–326.
- (65) Bohm, D. *Phys. Rev.* **1952**, *85*, 166–193.
- (66) Garashchuk, S.; Rassolov, V. A. *Chem. Phys. Lett.* **2002**, *364*, 562–567.
- (67) Garashchuk, S.; Rassolov, V. A. *Chem. Phys. Lett.* **2003**, *376*, 358–363.
- (68) Ehrenfest, P. Z. *Physik* **1927**, *45*, 455.
- (69) Gindensperger, E.; Meier, C.; Beswick, J. A.; Heitz, M. C. *J. Chem. Phys.* **2002**, *116*, 10051–10059.
- (70) Slater, J. C.; Koster, G. F. *Phys. Rev.* **1954**, *94*, 1498–1524.
- (71) Mermin, N. D. *Phys. Rev. A* **1965**, *137*, 1441.
- (72) Sokoloff, J. *Ann. Phys.* **1967**, *45*, 186–190.
- (73) Huang, J.; Jakowski, J.; Beste, A.; Younker, J.; Vazquez-Mayagoitia, A.; Cruz-Silva, E.; Fuentes-Cabrera, M.; Lopez-Bezanilla, A.; Meunier, V.; Sumpter, B. In *Practical Aspects of Computational Chemistry II*; Leszczynski, J., Shukla, M. K., Eds.; Springer: Netherlands, 2012; pp 209–278.
- (74) Weinert, M.; Davenport, J. W. *Phys. Rev. B* **1992**, *45*, 13709.
- (75) Wentzcovitch, R. M.; Martins, J. L.; Allen, P. B. *Phys. Rev. B* **1992**, *45*, 11372.
- (76) Press, W. H.; Flannery, B. P.; Teukolsky, S. A.; Vetterling, W. T. *Numerical Recipes: The Art of Scientific Computing*, 2nd ed.; Cambridge University Press: Cambridge, 1992.
- (77) Lee, C.; Yang, W.; Parr, R. *Phys. Rev. B* **1988**, *37*, 785–789.
- (78) Becke, A. J. *Chem. Phys.* **1993**, *98*, 5648–5652.
- (79) Shao, Y.; et al. *Phys. Chem. Chem. Phys.* **2006**, *8*, 3172–3191.
- (80) Irle, S., *private communication*.
- (81) Feit, M. D.; Fleck, J. A., Jr.; Steiger, A. J. *Comput. Phys.* **1982**, *47*, 412–433.
- (82) Kosloff, R. J. *Phys. Chem.* **1988**, *92*, 2087–2100.
- (83) Mazzuca, J.; Garashchuk, S.; Jakowski, J. *Chem. Phys. Lett.* **2012**, *542*, 153–158.
- (84) Garashchuk, S.; Volkov, M. V. *J. Chem. Phys.* **2012**, *137*, 074115.